DTU Library

Interplanetary magnetic field B$_x$ component influence on horizontal and field-aligned currents in the ionosphere

Laundal, K. M.; Reistad, J. P.; Finlay, C. C.; Østgaard, N.; Tenjord, P.; Snekvik, K.; Ohma, A.

Interplanetary magnetic field B_x component influence on horizontal and field-aligned currents in the ionosphere

K. M. Laundal[1] *, J. P. Reistad[1], C. C. Finlay[2], N. Østgaaard[1], P. Tenjord[1],

K. Snekvik[1], A. Ohma[1]

K. M. Laundal, karl.laundal@ift.uib.no

[1]Birkeland Centre for Space Science,

Department of Physics and Technology,

University of Bergen, Norway

[2]DTU Space, National Space Institute,

Technical University of Denmark, Kgs.

Lyngby, Denmark

*Funded by the Research Council of

Norway/CoE under contract 223252/ F50

Abstract.   Statistical analyses have shown that the sunward component of the interplanetary magnetic field, B_x (GSM), moderately but significantly affects the auroral intensity. These observations have been interpreted as signatures of a similar IMF B_x control on Birkeland currents, yet to be observed directly. Such a control, attributed to differences in magnetic tension on newly opened magnetic field lines, would lead to stronger region 1 (R1) Birkeland currents for B_x negative (positive) conditions in the northern (southern) hemisphere than when B_x is positive (negative). In this paper we perform a detailed investigation of three different sets of magnetic field measurements, from the CHAMP and *Swarm* low-Earth-Orbit satellites, from the AMPERE products derived from the Iridium satellite constellation, and from the SuperMAG ground magnetometer network, each analyzed using different techniques, to test these predictions. The results show that a change in sign of B_x changes the Birkeland currents by no more than $\approx$ 10%. The current patterns show little support for an inter-hemispheric asymmetry of the kind proposed to explain auroral observations. Instead we propose an alternative interpretation, which is consistent with most of the auroral observations and with the current observations in the present paper, except for those based on AMPERE: The solar wind-magnetosphere coupling is more efficient when the dipole tilt angle and B_x have the same sign than when they are different. We suggest the higher coupling is because the dayside reconnection region is closer to the subsolar point when the dipole tilt angle and B_x have the same sign.

Keypoints:

- Three different observational tests are carried out in search of B_x effects

on currents

- Only small differences are observed between different signs of B_x when

$B_z < 0$

- Observations indicate stronger SW-M coupling when B_x and dipole tilt

have the same sign.

1. Introduction

The orientation of the interplanetary magnetic field (IMF) is the most important factor governing energy transfer from the solar wind to the terrestrial magnetosphere [e.g., *Tenfjord and Østgaard*, 2013]. Among its three GSM components, the z component most strongly controls the energy transfer, since it largely determines whether or not the IMF and the Earth's magnetic field are anti-parallel. When they are, magnetic reconnection takes place, and solar wind kinetic energy can be converted to magnetic energy in the magnetosphere. When the IMF has a strong y component, which it usually does [*Wilcox and Ness*, 1965], magnetic tension on newly opened magnetic field lines diverts the subsequent flow of plasma differently in the two hemispheres, leading to significant asymmetries in the magnetosphere [*Tenfjord et al.*, 2015] manifested in global convection patterns [e.g. *Haaland et al.*, 2007; *Heppner and Maynard*, 1987; *Pettigrew et al.*, 2010], currents [e.g. *Green et al.*, 2009; *Anderson et al.*, 2008; *Laundal et al.*, 2016a], and auroral intensity [e.g. *Shue et al.*, 2001; *Newell et al.*, 2004]. The x component, on the other hand, is most often assumed to be unimportant. It is the purpose of this paper to investigate whether this assumption is true when it comes to ionospheric currents. By ionospheric currents, we mean both the horizontal and the field-aligned currents in the ionosphere, mapped to 110 km altitude. The study is restricted to situations when subsolar reconnection dominates; during predominantly northward IMF, B_x may have significant effects on lobe reconnection and associated dynamics [see e.g. *Østgaard et al.*, 2003; *Shi et al.*, 2013], which we do not discuss here.

When the IMF has a strong component in the Earth-Sun (x) direction, newly opened magnetic field lines will have a very different curvature. That difference translates to a hemispheric asymmetry in magnetic tension forces which, according to *Cowley* [1981], result in an induced magnetic x component in the magnetosphere with the same sign as the IMF B_x. Although this process is analogous to how B_y leads to hemispheric asymmetries, it is ostensibly of much less consequence for global geospace. We are only aware of few studies that investigate the global effects of IMF B_x observationally. One focuses on convection [*Förster et al.*, 2011] and the others on auroral intensities: *Shue et al.* [2002] reported global average patterns of auoral UV luminosity, observed by Polar Ultraviolet Imager (UVI) from above the northern hemisphere, showing stronger aurora when $B_x < 0$ than when $B_x > 0$ (when $B_z < 0$). Based on Polar UVI observations from January 1997, *Baker et al.* [2003] reached similar conclusions. *Reistad et al.* [2014], motivated by observations from single events showing non-conjugate aurora during strong B_x conditions [*Laundal and Østgaard*, 2009; *Reistad et al.*, 2013], did a statistical analysis of UV auroral images from the Wideband Imaging Camera (WIC) on the IMAGE satellite, in search of B_x effects. Their observations, which focused on the dusk region, showed a weak but statistically significant anti-correlation between B_x and auroral intensity in the north, and a correlation in the south. Both *Shue et al.* [2002] and *Reistad et al.* [2014] explained their findings in terms of corresponding asymmetries in upward field-aligned currents, which are carried in part by the downward electrons that excite auroras. In terms of the average picture first discovered by *Iijima and Potemra* [1978], these upward currents are the region 1 current at dusk and region 2 current at dawn, the former being the strongest.

Even though *Shue et al.* [2002] and *Reistad et al.* [2014] observed the same B_x dependence, and explained their findings in terms of current asymmetries inferred from the *Cowley* [1981] picture, their arguments for how this picture implies asymmetric currents differed. According to *Reistad et al.* [2014], the geometry suggested by *Cowley* [1981] on newly opened field lines during strong IMF B_x implies different magnetopause currents above the polar regions. Their conjecture was that this asymmetry also affects the region 1 currents, which in turn controls the auroral intensity. The effect of different field line curvature presumably decreases as the open field lines travel far down-tail, consistent with observations of strongest asymmetries at magnetic local times earlier than 20. The effect should be present also in the dawn region 1 current, although this is not manifested in electron auroras. It is not clear how or if differences in magnetopause currents affect region 2 currents. *Shue et al.* [2002], on the other hand, argued from a purely geometrical point of view: An induced B_x in the magnetosphere will shift the footpoints of magnetospheric field lines towards or away from the sun, the direction depending on B_x and hemisphere. This shift was thought to increase or decrease ionospheric flow shears, with corresponding changes in Birkeland currents. As a consequence, *Shue et al.* [2002] predict stronger R1 currents on the nightside in the northern hemisphere when B_x is negative, similar to *Reistad et al.* [2014], but they predict the opposite asymmetry in the dayside part of the R1 current. Furthermore, they predict a B_x-dependent asymmetry in the R2 current which is similar to the asymmetry in the adjacent R1 current.

To our knowledge, no direct observations of currents have been presented to test these predictions. This is what we undertake in this paper. Since the B_x effects, if they exist, are weak, it is an advantage to consider multiple tests using different datasets. In the

next section we start by presenting the results from an empirical model of ionospheric currents, specifically designed to reveal asymmetries associated with IMF B_x, based on magnetic field observations from the CHAMP and *Swarm* satellites (Section 2.1). Then we present statistics based on the Active Magnetosphere and Planetary Electrodynamics Response Experiment (AMPERE), which offers global Birkeland current maps based on magnetometers on the Iridium satellites (Section 2.2). Finally, we present global maps of the equivalent horizontal current, calculated using ground magnetometers (Section 2.3). In section 2.4 we present a summary of all the tests. In Section 2 we focus primarily on the predictions made by *Reistad et al.* [2014], but return to discuss our results in terms of the *Shue et al.* [2002] predictions in section 2.4. In Section 3 we discuss the implications of our findings, and Section 4 concludes the paper.

In order to isolate the effect of the IMF B_x, a number of biases must be considered. The interplanetary magnetic field lines typically form a spiral, called the Parker spiral [*Parker*, 1958]. Parker spiral IMF vectors at 1 AU are either towards the Sun and along Earth's orbit, or away from the Sun and opposite to Earth's orbit. This means that the GSM B_x and B_y components are significantly correlated; we calculate a correlation coefficient of -0.39 using $> 12 \cdot 10^6$ 1 min OMNI data points from 1981 to 2016. In addition, there is a seasonally dependent correlation of the IMF B_y (and thus B_x) with geomagnetic activity: Near spring equinox, geomagnetic activity is larger when B_y is negative than when it is positive. In the fall, the situation reverses. This was demonstrated by *Zhao and Zong* [2012]. They explained the annual variation in correlation between B_y and geomagnetic activity as an aspect of the more fundamental Russell-McPherron (R-M) effect [*Russell and McPherron*, 1973]. The R-M effect is a semiannual and diurnal variation in geomag-

netic activity due to variations in the orientation of Earth's magnetic field with respect to the Parker spiral interplanetary magnetic field. The basic idea is that the Parker spiral magnetic field is in the xy plane in Geocentric Solar Equatorial (GSEQ) coordinates, and that its projection on the yz plane in Geocentric Solar Magnetospheric (GSM) coordinates changes. It should be noted, considering the topic of the present paper, that the x component is the same in GSEQ and GSM coordinates, and is not directly part of the R-M effect. Nevertheless, the Parker spiral orientation and the seasonal variations of the R-M effect mean that the most important controlling parameters for ionospheric currents are strongly correlated. Because of these correlations between controlling parameters, we severely constrain the data selections in the observations presented below, in order to minimize the contribution from other parameters, in particular the IMF B_y. Possible biases are also considered in detail in Appendix A. In Appendix B, we present the same figures as in Section 2, except that the roles of B_x and B_y are reversed. The purpose of this is to demonstrate that our techniques are capable of reproducing known variations in currents with B_y. That indicates that they would also be capable of isolating B_x effects, if these exist.

2. Observations

In this section we present tests of the B_x effect using three different datasets. For each dataset, we present global average patterns of Birkeland currents and/or equivalent currents, but the techniques used to calculate the averages differ. We use only data from periods when B_z was negative, which implies favorable conditions for subsolar reconnection and less so for lobe reconnection. Also, each dataset is split in two disjoint sets, defined by the dipole tilt angle being either $< -10°$ or $> 10°$. This is done in order to

reveal potential seasonal dependencies (the results by *Reistad et al.* [2014] were based only on winter observations), and also to increase the number of tests based on statistically independent data points. Each set is used to provide independent comparisons between corresponding average currents for different signs of B_x. Apart from visually comparing the morphology of the current, we use peak current values as a metric for quantitative comparison of Birkeland currents.

2.1. Test 1: CHAMP and *Swarm*

Thanks to the CHAMP and *Swarm* satellite missions, we now have access to many years of incredibly precise measurements of the magnetic field at low Earth orbit, providing global coverage for studies of a large range of external conditions. This dataset is therefore an ideal basis for climatological models of global ionospheric currents. Here we present results from two such models, parametrized in terms of the orientation of the interplanetary magnetic field. The two models are based on data from periods when then dipole tilt was either $> 10°$ or $< -10°$, respectively. The data was sampled at 30 sec cadence, and a high resolution model of the near-Earth (main) geomagnetic field, CHAOS-6 [*Finlay et al.*, 2016] was subtracted. CHAOS-6 includes estimates of the core field, the lithospheric field, and the quiet-time near-Earth field due to magnetospheric currents.

The remaining field, $\Delta\mathbf{B}$, is a sum of poloidal and toroidal parts, which can be written in terms of scalar fields V and T, respectively [e.g., *Backus*, 1986; *Olsen*, 1997]:

$$\Delta\mathbf{B} = -\nabla V + \mathbf{r} \times \nabla T, \tag{1}$$

where $\mathbf{r}$ is a radial vector. V relates to currents that do not intersect the satellite orbits (including divergence-free horizontal currents in the ionosphere), and T relates to currents

that cross the the orbits (i.e., the field-aligned currents). We express V and T in terms of spherical harmonics, defined in apex quasi-dipole (QD) and modified apex (MA) coordinates [*Richmond*, 1995a], respectively, with magnetic local time [*Laundal and Richmond*, 2017] as the azimuthal coordinate. We take the non-orthogonality of these coordinate systems into account when evaluating the gradients in (1). The technique is described in detail and demonstrated by *Laundal et al.* [2016b], who applied it to datasets binned by solar wind and seasonal conditions. We refer to that paper for a detailed mathematical description. Here we extend the technique by allowing the spherical harmonic coefficients to vary as a function of the IMF and solar wind velocity.

The nature of the relationship between spherical harmonic coefficients and these external parameters is not trivial. *Weimer* [2013] found that, for a general model of ground magnetic field perturbations, it was beneficial to use a Fourier expansion in IMF clock angle θ_c (the angle between the IMF in the yz plane and the GSM z axis), scaled by various terms thought to influence the currents (tilt angle, solar wind velocity, IMF magnitude, and $F_{10.7}$). Inspired by this, we choose a similar function, adapted for our purposes. Each spherical harmonic coefficient in the expansion of V and T [see equations 7 and 9 of *Laundal et al.*, 2016b], say g_n^m, is expanded as

$$g_n^m = a_n^m + b_n^m \epsilon + c_n^m \epsilon \cos(\phi) + d_n^m \epsilon \sin(\phi) + e_n^m \epsilon \cos(2\phi) + f_n^m \epsilon \sin(2\phi). \qquad (2)$$

This is a Fourier expansion in IMF azimuth angle, ϕ, scaled by a solar wind coupling function, ϵ. The azimuth angle is defined as the angle between the IMF in the xy plane and the GSM x axis. The ϵ parameter used here is that proposed by *Newell et al.* [2007], $\epsilon = |v_x|^{4/3} B_{yz}^{2/3} \sin^{8/3}(\theta_c/2)$, where v_x is the solar wind velocity in the GSM x direction, B_{yz} is $\sqrt{B_y^2 + B_z^2}$. The numerical values of ϵ reported in this paper are calculated with v_x in

units of km/s, B_{yz} in units of nT, and then scaled by 10^{-3}. The key property of ϵ is that it presumably correlates well with dayside reconnection rate, although its unit is physically meaningless and therefore not reported. We only use data from periods when $B_z < 0$. The solar wind and IMF parameters are determined from 1 min OMNI data, averaged over the 20 min prior to the time of the corresponding *Swarm*/CHAMP measurement. In total we use 8,211,033 measured vector components to determine the coefficients of the model for negative tilt angles $(< -10°)$, and 9,195,507 components for the positive tilt angle model $(> 10°)$. The CHAMP measurements are from August 2000 to September 2010, and *Swarm* from December 2013 to August 2016.

The spherical harmonic series are truncated at $n, m = 35, 5$ for V and at $n, m = 60, 5$ for T. That leads to 1005 real coefficients which are each expanded in terms of the 6 parameters of equation 2. This equation, together with equations 10, 11, and 12 in *Laundal et al.* [2016b] relate a vector of measurements, $\mathbf{d}$ to a vector of 6030 model coefficients, $\mathbf{m}$. The full set of equations can be formulated as a matrix equation, $\mathbf{Gm} = \mathbf{d}$, where $\mathbf{m}$ can be estimated using an iteratively re-weighted least-squares scheme that robustly handles long-tailed distributions of data errors. In the $(i + 1)$'th iteration, $\mathbf{m}_{i+1}$ is determined by

$$\mathbf{m}_{i+1} = (\mathbf{G}^T \mathbf{W}_i \mathbf{G} + \alpha \mathbf{R})^{-1} \mathbf{G}^T \mathbf{W}_i \mathbf{d} \tag{3}$$

where $\mathbf{W}_i$ is a weight matrix which depends on the misfit in the i'th iteration, $\mathbf{e}_i = \mathbf{Gm}_i - \mathbf{d}$. The diagonal elements of $\mathbf{W}_i$ are called Huber weights [*Huber*, 1964], and are defined as

$$W_{jj} = \min(1, 1.5\sigma/|e_i^j|), \tag{4}$$

where e_i^j is the j'th element of $\mathbf{e}_i$ (a vector with as many elements as there are measurements). σ is in this case determined as the square root of the Huber weighted mean squared element of $\mathbf{e}_i$. In addition to the variable weights, we weight observations from the side-by-side flying satellites, *Swarm* Alpha and Charlie, by 0.5, since they are assumed not to provide independent information on the length scales considered by our model.

The inversion in equation 3 is done by use of Cholesky decomposition, and the Python Scipy function cho_solve, which makes use of the LAPACK library [*Anderson et al.*, 1999]. This technique fails unless we apply some regularization for the toroidal field. The reason for that is probably that the representation in modified apex coordinates is not appropriate for low latitudes [*Matsuo et al.*, 2015], and a lack of coverage near the modified magnetic apex equator, which is at the dip equator at the chosen reference height, 110 km [see *Richmond*, 1995a, for details]. Therefore the regularization matrix $\mathbf{R}$ in equation 3 is chosen to measure the mean square vector toroidal field due to the field aligned currents [see e.g., *Sabaka et al.*, 2010, equation 116] and is a diagonal matrix, with elements $\alpha n(n+1)/(2n+1)$ in the columns that correspond to the elements of $\mathbf{m}$ that are coefficients in the expansion of T, and zero otherwise. α was set to 100, the smallest power of 10 that prevented cho_solve from failing. No regularization is used for V. The iterations were terminated when $\|\mathbf{m}_i - \mathbf{m}_{i+1}\| < 0.04\|\mathbf{m}_0\|$. This occurred after 7 iterations in the negative tilt angle model, and 6 iterations for the positive tilt angle model.

The iterative scheme progressively down-weights outlying data points that deviate strongly from model values. This procedure reduces the impact of such outliers, and enables the final solution to better represent typical values rather than simple mean values. The misfit in the final iterations, as quantified as the root Huber weighted mean

square element of **e**, was 17.2 nT in the negative tilt angle model, and 16.2 nT in the positive tilt angle model. The root mean squares of the data points for the corresponding models were 62.1 nT and 57.1 nT, respectively. The mean Huber weight in the final iteration was 0.87 for both models.

The curl of equation 1 gives the currents associated with $\Delta\mathbf{B}$. From T we can analytically calculate field-aligned currents at some height (we use 110 km). From V we can calculate the divergence-free part of a horizontal current sheet under the satellite orbits, also assuming a height of 110 km. We represent the divergence-free sheet current density $\mathbf{j}_{df}$ in terms of a scalar current function Φ: $\mathbf{j}_{df} = \mathbf{k} \times \nabla\Phi$, where $\mathbf{k}$ is an upward unit vector. The divergence-free current function is very similar to the equivalent current function derived with ground magnetometers (we return to this in Section 2.3). Equations relating the spherical harmonic coefficients in the expansion of $\Delta\mathbf{B}$ to currents can be found in *Laundal et al.* [2016b, see their equations 15 and 16].

Figure 1 shows Birkeland currents and equivalent currents in the northern and southern hemispheres from the two models for positive and negative tilt angles. To produce this figure we have evaluated the model setting $\epsilon = 4$, which is close to the peak of the distribution of ϵ in the two datasets. We also set $B_y = 0$, to highlight differences related to B_x. $\epsilon = 4$ and $B_y = 0$ could correspond to a solar wind speed of about 290 m/s, and $B_z = -3$ nT. The negative dipole tilt angle model is shown in the two columns to the left, and the positive dipole tilt model is shown in the columns to the right. The two upper rows represent northern hemisphere patterns and the two lower rows represent southern hemisphere patterns.

B_x effects should appear as differences between horizontal image pairs in the two model columns. It is immediately clear from visual inspection that any such differences are small. This is in contrast to the IMF B_y, which has a pronounced influence on current morphologies [*Weimer*, 2001; *Anderson et al.*, 2008; *Green et al.*, 2009; *Laundal et al.*, 2016a].

The numbers in the lower right corners of the Birkeland current plots in Figure 1 correspond to the peak current values, in μA/m^2. The maxima consistently correspond to peak upward R1 currents (dusk), and the minima correspond to peak downward R1 currents (dawn). Comparing corresponding peaks between the horizontal pairs, we find that 4 out of 8 are slightly asymmetrical in the direction predicted by *Reistad et al.* [2014] (stronger R1 currents for $B_x < 0$ in the north, and opposite in the south), while the remaining pairs show the reverse. All differences are however rather small, being only about 10%. We note that all winter hemisphere asymmetries are consistent with the *Reistad et al.* [2014] predictions, while the summer hemisphere results are not. We return to this seasonal difference in B_x dependence in the discussion section.

Figure 1 only shows the asymmetries for cases when $\epsilon = 4$. The arguments presented by *Reistad et al.* [2014] suggest that stronger solar wind velocity, and stronger magnetic field, will enhance the asymmetry. In Figure 2 we test if the asymmetries become clearer when ϵ increases. The figure presents the ratios of corresponding R1 currents for different signs of B_x as a function of ϵ. The ratios are defined such that they are greater than 1 if the *Reistad et al.* [2014] predictions are fulfilled. We see that as ϵ becomes very large, 6 out of 8 ratios are > 1, supporting the predictions. However, we emphasize that large values for ϵ are rare in the dataset used to make the model, as shown in the normalized

distributions in Figure 2C, and the models presumably become similarly more uncertain in this extreme regime.

In addition to the Birkeland currents, Figure 1 also shows equivalent ionospheric currents. It is not obvious how the B_x effect would be expected to affect equivalent current, except that when B_x favors strong R1 currents the equivalent currents should be stronger too. From visual inspection, there is no appreciable difference in the estimated equivalent currents between B_x positive and negative conditions. However, in all but one case, the total current, given in the lower right corners, is slightly stronger when the *Reistad et al.* [2014] predictions indicate stronger currents. The only case where this is not true is in the northern hemisphere for tilt $> 10°$ (Figures 1G and 1H), where the difference is less than 1%.

We have chosen not to focus on hemispheric differences in Figure 1, even though in principle we could compare the negative (positive) tilt model in the northern hemisphere to the positive (negative) tilt model in the south to look for inter-hemispheric B_x effects. The reason for this is that there are inherent asymmetries between hemispheres, that could easily contribute differences of similar magnitudes as the effect of B_x. The most important hemispheric asymmetries are different offsets between geographic and magnetic poles, and different field strengths. Differences in pole offset lead to different variations in insolation, and thus conductivity, in the two hemispheres, which are not fully described by the dipole tilt angle [*Laundal et al.*, 2016a]. Differences in magnetic field strength also lead to differences in ionospheric conductivity directly through its influence on ionospheric plasma [*Richmond*, 1995b; *Cnossen et al.*, 2012], and indirectly through variations in the particle mirror height, changing the flux of ionizing particle precipitation [*Stenbaek-Nielsen et al.*,

1973]. These differences may remain important even after compensating for geometric differences in the main field which we do here by use of magnetic apex coordinates. See *Laundal et al.* [2017] for a review of how north-south asymmetries in the main field may affect geospace phenomena.

2.2. Test 2: AMPERE maps of field aligned currents

Figure 3 shows global average Birkeland currents, calculated using AMPERE maps from between January 2010 and May 2013. AMPERE provides polar maps of field-aligned currents at 2 min cadence and 10 min integration time, based on magnetometer measurements from the fleet of commercial Iridium satellites and spherical harmonic analysis [*Waters et al.*, 2001; *Anderson et al.*, 2000]. The plots in Figure 3 differ by data selection criteria: The top rows are based on data from the northern hemisphere, and the bottom from the southern hemisphere. The two columns to the left are based on data from periods when the tilt angle was $< -10°$, and the right plots on periods when the tilt angle was $> 10°$. In addition, the columns correspond to different signs of B_x, as indicated above the top row plots. For all the plots, $B_z < 0$ nT, $|B_x| > 2$ nT and $|B_y| < 1$ nT, ensuring strong solar wind coupling, and little contamination from B_y effects. Each map was also subject to a stability selection criterion, based on the similarity with the map from 20 min earlier. We use the same similarity metric as *Anderson et al.* [2008], the fractional overlap, which we require to be > 0.45.

The final number of maps available for calculating the average is given in the lower left corner of the plots. The average was calculated in a robust way, using Huber weights, largely analogous to what was done for the model estimation in the previous section: We start by calculating the simple mean map and standard deviation map. Then, for each

map, we make a map of weights, which are 1 if the distance from the mean is less than 1.5 in units of the standard deviation, and decreasing in inverse proportion to that distance for larger deviations. These weights are used in a new iteration to calculate an updated weighted mean. The corresponding weights are then also updated and new mean maps again calculated until the difference from the previous iteration is small. This robust procedure helps to reduce the impact of outliers.

Visual inspection of Figure 3 reveals no clear difference between different signs of B_x. Investigating the peak R1 values, we find that 6 out of 8 have an asymmetry in the direction predicted by *Reistad et al.* [2014]. Among those are the largest difference found in this study, a 38% stronger peak R1 current at northern dusk when the tilt angle is $< -10°$. Thus the AMPERE results are slightly more supportive of the *Reistad et al.* [2014] predictions than the analysis based on *Swarm* and CHAMP data, although the interpretation of the results is not without ambiguity.

2.3. Test 3: SuperMAG ground magnetometers: Equivalent currents from binned averages

As a final test of the B_x influence, we present equivalent current patterns based on ground magnetometer measurements. The ground magnetometer measurements are processed and made available by SuperMAG [*Gjerloev*, 2012]. The SuperMAG measurements were obtained in the years 1981-2014, converted to QD coordinates [*Laundal and Gjerloev*, 2014; *Laundal et al.*, 2016a], binned in 920 grid cells, sorted according to the IMF orientation, $B_z < -1$ nT, $|B_y| < 1$ nT, B_x and tilt angle $> 10°$ or $< -10°$, and averaged taking the simple mean. The average vectors were then fitted with a spherical harmonic representation of external and internal magnetic potentials as described by *Laundal et al.*

[2016a]. The external magnetic potential corresponds to ionospheric currents, but it can not be used to derive the full 3-dimensional current system without any additional information. Instead, we use it to calculate an equivalent current, a sheet current in a spherical shell at 110 km that would produce a magnetic field that is equal to the observed external field. We represent the equivalent current in terms of a scalar Ψ, analogous to the divergence-free current function derived from space: $\mathbf{j}_{eq} = \mathbf{k} \times \nabla\Psi$, where $\mathbf{j}_{eq}$ is the horizontal equivalent sheet current density. We refer to *Laundal et al.* [2016a] for a detailed description of how Ψ is estimated, and to *Laundal et al.* [2016b] for a discussion about the differences between the equivalent current function Ψ and the current function Φ, derived with satellite magnetometers. Figure 4 shows contour plots of the equivalent current function associated with the external magnetic potential. The total current flowing between the maximum and minimum of the current function is given in the lower right corners. The root-mean-square error of the spherical harmonic fit is given in the lower left corners. The top right corners indicate the total number of SuperMAG measurements that were used to make each plot. Only patterns from the northern hemisphere are shown, since the ground magnetometer coverage is much better there.

Visual inspection reveals little difference between currents for different signs of B_x. The difference in total current is in the order of 5%. The difference is consistent with the *Reistad et al.* [2014] predictions during negative tilt, but not during positive tilt.

2.4. Summary of results

We have presented maps of ionospheric currents from three different data sources, using three different techniques. The maps offer several opportunities to compare currents in search of differences related to the IMF B_x component. We can conclude already, based

on visual inspection of the maps, that any B_x influence must be small, of the order of $\approx 10\%$.

We have used the ratios between corresponding peak currents as a quantitative metric of the B_x associated asymmetries. The ratios are not unambiguously in the direction suggested by the *Reistad et al.* [2014] predictions. Figure 5 shows all the ratios, visualized as increasingly red or blue dots, depending on the sign of the differences. Red dots indicate asymmetries that are consistent with *Reistad et al.*'s predictions for the B_x effect. There are slightly more red dots than blue dots, but there is no evidence for a very strong influence of B_x.

So far we have focused on the B_x predictions made by *Reistad et al.* [2014]. However, as mentioned in the introduction, *Shue et al.* [2002] interpret the *Cowley* [1981] picture somewhat differently, leading to a different set of predictions for how B_x affects field-aligned currents: In the northern hemisphere, both the R1 and R2 currents should be stronger on the night side when $B_x < 0$, but they should be weaker on the dayside. In the southern hemisphere, the variation is reversed. These differences arise because of a shift in the sun-Earth direction of the polar magnetic field line footpoints, due to a perturbation in the magnetosphere in the x direction. That shift compresses or expands the circulation patterns in the ionosphere, leading to stronger and weaker currents, respectively.

Figure 6 is produced to highlight the variations predicted by *Shue et al.* [2002], if they exist. It shows the peak upward (positive) and downward (negative) currents, from Figures 1 and 3, as a function of MLT. Currents corresponding to B_x positive conditions are shown as solid blue curves, and B_x negative as dashed curves. If the predictions are true, there should be clear differences between the solid and dashed lines in Figure 6, and

the difference should change sign once in each quadrant. The asymmetry should also be opposite between northern and southern hemispheres. This behavior is not seen. Instead, we see that the peak currents during different directions of B_x have remarkably similar variations with MLT. Consequently, we conclude that the effect predicted by *Shue et al.* [2002] is either very weak or non-existent.

3. Discussion and conclusions

Our analysis shows that the IMF B_x component has very little or no influence on ionospheric currents when the IMF B_z is southward. In arriving at these results, we have taken great care to constrain the B_y component, which otherwise would have contaminated the results because of the Parker spiral configuration of the interplanetary magnetic field. We have also utilized three different datasets, and divided those datasets into disjoint sets, which gives several independent assessments of the B_x influence. In the parametrized current model (Section 2.1) and for the average AMPERE maps (Section 2.2) we used iterative schemes to reduce the effect of outliers, although similar conclusions are also reached using less sophisticated techniques based on simple mean values. Despite the constraints on B_y, and use of robust statistics, potential biases remain: 1) For both *Swarm*/CHAMP and AMPERE, there may be differences in dipole tilt angle distributions within the data bins, and 2) for AMPERE, the solar wind magnetosphere coupling may be systematically different in the different bins. The latter is not a concern for the CHAMP/*Swarm* results, since any bias should be handled by the ϵ parameter in equation 2. We address these concerns in in appendix A, and show that the mentioned biases do not change the conclusions of the paper.

In the rest of this section, we briefly review previous literature on the topic of B_x influence on polar ionospheric electrodynamics in the context of the present findings (sections 3.1 and 3.2). Then, in section 3.3, we present an alternative interpretation of the result, which does not involve inter-hemispheric asymmetries, but still explains the findings by *Reistad et al.* [2014] and most of the B_x related differences reported in the previous sections.

3.1. Relation to previous studies

The observed small variation with B_x are consistent with the only study that we are aware of that looks for B_x effects in ionospheric convection: *Förster et al.* [2011] used Cluster observations, mapped to the ionosphere along model magnetic field lines, to derive global maps. By binning their data according to IMF orientation, they showed that B_x had very little influence when $B_z < 0$. Interestingly, there did seem to exist a B_x dependence when B_z was northward. That is consistent with auroral observations by *Elphinstone et al.* [1990], and by *Østgaard et al.* [2003], who argued that B_x changes magnetic field geometries such that lobe reconnection rates are not balanced between hemispheres. Lobe reconnection is believed to be minimal in the data used in the present study, since we require B_z to be negative and B_y small.

Our results also appear to be consistent with the numerical simulations by *Peng et al.* [2010], which showed no hemispheric asymmetries in ionospheric electric potential as B_x increased. Only in the outer magnetosphere did B_x lead to north-south asymmetries. The magnetopause position, bow shock position, and reconnection site all became asymmetrical between hemispheres, although only for the relatively uncommon case of low solar wind Alfven Mach number. Under such conditions, *Peng et al.* [2010] also found that

increasing B_x leads to reductions in cross polar cap potential in both hemispheres. In section 3.3 we discuss how this finding can be reconciled with our results.

3.2. Asymmetries in the aurora associated with B_x

Taken at face value, our results seem to contradict the findings by *Shue et al.* [2002] and *Reistad et al.* [2014], who found that B_x has a small but significant influence on auroral intensity. This influence was explained in terms of ionospheric currents, controlled by B_x through mechanisms analogous to how B_y affects the magnetosphere [*Cowley*, 1981].

Because of this discrepancy, we should consider the possibility that the observations by *Shue et al.* [2002] and *Reistad et al.* [2014] of B_x-dependent asymmetries do not reflect a true B_x control, due to observational and/or technical issues. While we are not able to point out any specific problems in these studies, this conclusion can not be ruled out. It is well known that the space based UV imagers that were used are prone to variations that are difficult to fully account for in statistical studies, and which may lead to hidden biases. Especially the results by *Shue et al.* [2002] from the northern hemisphere summer season might be questioned, due to the impact of sunlight on UV auroral images, and the difficulty in correcting for this contamination. As we will show below, if we disregard this last observation, the auroral observations can be reconciled with most of the current observations in the present paper if the interpretation is changed. However, considering the small magnitudes of the observed B_x variations, we suggest testing the auroral observations with other, independent datasets, for example the particle and/or optical instrumentation on-board the DMSP satellites.

A second possible explanation for the discrepancy may have to do with a seasonal difference in the magnitude of the B_x asymmetries. In the pre-midnight region, there

seems to be a non-linear relationship between current and aurora, where increasing auroral intensity ionizes the atmosphere, leading to increasing currents, which in turn increases the aurora [see e.g., *Ohtani et al.*, 2009]. This amplifying effect in darkness may be the reason why only 2 out of 11 comparisons from the winter hemisphere in Figure 5 are inconsistent with the *Reistad et al.* [2014] predictions. However, it is puzzling that the CHAMP/*Swarm* results consistently show an opposite asymmetry of similar magnitude during local summer. In the next section we present a new interpretation which explains this, as well as additional evidence which is more in line with this new idea rather than nightside amplification.

3.3. Increased geoefficiency when B_x and dipole tilt have the same sign

A third interpretation of the discrepancy between the auroral observations and the observations in the present paper is possible: That the observations by *Shue et al.* [2002] and *Reistad et al.* [2014] about B_x dependent auroras reflect a real difference, but their interpretation in terms of hemispherically asymmetric currents is wrong. This conclusion calls for an alternative mechanism. Here we propose that the dominating effect of B_x in this and the previous studies is to change the overall coupling efficiency between the solar wind and the magnetosphere, allowing more energy to be transferred when B_x and the dipole tilt have the same sign.

We suggest that the mechanism behind this effect is related to how the dipole tilt angle and B_x affect the location of the dayside reconnection site: Models [*Russell et al.*, 2003; *Park et al.*, 2006; *Hoilijoki et al.*, 2014] and observations [*Zhu et al.*, 2015] show that the dayside reconnection site shifts southward (northward) of the subsolar point when the dipole tilt angle is positive (negative). That is, the reconnection site tends to follow the

Earth's equatorial plane as it tilts away from the Sun-Earth line. *Hoilijoki et al.* [2014] showed that B_x can equalize this shift, if it has the same sign as the tilt angle. Under such conditions, the reconnection site will be located near the subsolar point, where it is most efficient [*Park et al.*, 2006].

This idea is consistent with the results by *Reistad et al.* [2014], who observed stronger aurora (in the north) when B_x and dipole tilt was negative, compared to B_x positive conditions, and stronger aurora (in the south) when B_x and dipole tilt was positive, compared to B_x negative conditions. As mentioned before, this can be interpreted both as an inter-hemispheric asymmetry imposed by B_x which is independent of seasons, or, as we do here, an influence of B_x on the overall geoefficiency, which changes with the sign of the dipole tilt angle. *Shue et al.* [2002] reported B_x asymmetries from the northern hemisphere during both winter and summer. The new idea is only consistent with their winter results, but, as mentioned above, there are reasons to place less emphasis on the summer results due to the contamination of sunlight on the images.

This idea is also consistent with all the Birkeland current asymmetries observed in the CHAMP/*Swarm* models. It is also consistent with most of the horizontal current maps, from CHAMP/*Swarm* and SuperMAG: Only 1 out of 6 shows an inconsistent asymmetry, and 1 shows no asymmetry. The main discrepancy with this interpretation is found in the AMPERE comparisons, with only 2 out of 8 comparisons in agreement. There may however be reasons to place less emphasis on the AMPERE comparisons than the CHAMP/*Swarm* results. The AMPERE currents are derived from magnetometers that are much less accurate than those flying on CHAMP and *Swarm*, a shortcoming which is not necessarily compensated by the much greater number of spacecraft. Furthermore,

the distribution of orbits in magnetic coordinates may create complications in the current estimates which affect the results, especially in the southern hemisphere [*Anderson et al.*, 2017], where none of the comparisons happen to fit the new explanation.

If the solar wind-magnetosphere coupling is stronger when dipole tilt and B_x are in the same direction, other indicators of geomagnetic activity should be affected as well. In Figures 7 and 8 we test this concept on the AL index and on substorm occurrence, respectively.

Figure 7 shows binned averages of AL, plotted against binned average B_x. The bins are defined by $|B_y| < 1$ nT, $B_z < -1$ nT, dipole tilt angle either $< -10°$ (top) or $> 10°$ (bottom), and a set of quantiles for B_x during these conditions. That means that the bins contain an almost equal number of samples but that their B_x boundaries are variable. The averages are computed robustly, with iterative reweighting by Huber weights. The x axis shows the absolute value of B_x, and corresponding values of AL are labeled by $+$ or $-$ (blue and orange, respectively), depending on the sign of B_x. The figure clearly shows that AL tends to be stronger if B_x and the tilt angle have the same sign. This is consistent in all bins beyond $|B_x| \approx 2.5 nT$. Each bin is based on independent datapoints, with more than $> 12,000$ samples per point in both panels. The dataset, from the OMNI database, covers the period 1990-2016.

The difference does not seem to increase with increasing B_x, and it even decreases slightly with increasing B_x when the tilt angle is positive. It is possible that the effect maximizes for some angle between the IMF in the xz plane and the dipole axis. It may be that larger B_x over-compensates for the shift in reconnection region associated with the dipole tilt, and thus reduces the coupling efficiency. We note that this behaviour is

different from what we would expect from the *Reistad et al.* [2014] and *Shue et al.* [2002] mechanisms, which is that increasing B_x increases asymmetries.

If B_x affects the dayside reconnection rate in the manner proposed here, we should expect more substorms to occur when B_x and the tilt angle have the same sign. This is because more magnetic flux will be opened, and more substorms are therefore required to close it. We test this prediction in Figure 8, which is based on the SuperMAG substorm list [*Newell and Gjerloev*, 2011]. It shows the distribution of B_x during substorm onsets that happened between 1981 and 2016, when $|B_y| < 1$ nT, $B_z < -1$ nT, and the dipole tilt was either $< -10°$ (orange) or $> 10°$ (blue). Each distribution is based on more than 1500 substorms. The distributions are clearly asymmetrical, with positive B_x favored when the dipole tilt was positive, and negative B_x when the tilt angle was negative. This result is also different from what we would expect from the *Reistad et al.* [2014] and *Shue et al.* [2002] mechanisms, which do not involve any change in overall solar wind coupling efficiency. The result supports the idea that the dayside reconnection rate is stronger when the IMF B_x and the dipole tilt angle have the same signs, than when they are opposite.

4. Conclusions

We have shown through various observations that B_x leads to very small or negligible inter-hemispheric differences in ionospheric currents. This contradicts interpretations made in previous studies, to explain observations of B_x dependent asymmetries in the aurora.

While our results contradict previous predictions about inter-hemispheric differences associated with B_x, they do suggest a small and seasonally dependent influence of B_x

on the efficiency of the solar wind-magnetosphere coupling. This coupling tends to be stronger when B_x and the dipole tilt angle have the same sign. Under such conditions, the subsolar reconnection site is closer to the subsolar point [e.g. *Hoilijoki et al.*, 2014], and presumably more efficient.

The idea of a B_x-dependent coupling efficiency is supported by observations of average AL magnitudes, and of substorm occurrence. However, contradictory observations are also found, notably with AMPERE and in the observations by *Shue et al.* [2002] in the summer hemisphere. There is therefore a need for further investigations on this topic, with independent data sets, and on different quantities, such as ionospheric convection. There is also a need for a more detailed investigation of how the solar wind Alfven Mach number might change the B_x effect; the modeling by *Peng et al.* [2010] suggest that it becomes less important when the Mach number is large.

The B_x effect observed here is not, as far as we know, part of any solar wind magnetosphere coupling function [e.g. *Newell et al.*, 2007; *Tenfjord and Østgaard*, 2013, and references therein]. Our findings suggest that significant improvements can be made by taking it into account.

Appendix A: Potential biases in the datasets

Figure 9 shows the distribution of the *Newell et al.* [2007] coupling function, ϵ, across the maps used to produce the average currents of Figure 3. Significantly different distributions are expected to be associated with different current strengths, due to differences in solar wind-magnetosphere energy transfer. This could potentially obscure any B_x effect. The figure shows that the distributions are not identical, with more events having large values of ϵ when $B_x > 2$ nT and the dipole tilt angle (denoted by β in the figure) was $> 10°$. The observed differences with respect to B_x (Figure 3) are in the opposite direction, however, which suggests that this bias is not a major influence.

Figure 10 is produced to reveal any biases in dipole tilt angle distributions that might influence the comparisons of different B_x conditions using Figures 1 and 3. Figure 10A (B) shows the distributions of the dipole tilt angle at the times of the AMPERE maps used to make Figure 3C and 3D (3E and 3F). The distributions in Figure 10A are quite similar, showing that comparisons between Figures 3C and D are not influenced by tilt angle. The distributions in panel B are slightly skewed towards more sunlit conditions, and thus higher conductivities, for periods when $B_x > 2$ nT compared to $B_x < -2$ nT. This small bias possibly enhances the apparent B_x effect suggested by comparing figures 3E and 3F. Figure 10C shows the weighted mean absolute tilt angle, in $45°$ wide bins of IMF azimuth angle, ϕ, at the times of the CHAMP/*Swarm* data points that were used to produce Figure 1. The weights are the Huber weights of the last iteration in the iterative scheme used to estimate the model parameters. The essentially flat curves show that the results of the analysis in Section 2.1 are not influenced by biases in dipole tilt angle distributions.

Appendix B: By effects

This paper is mainly concerned with B_x effects. Since there is a significant anti-correlation between B_x and B_y, we have had to control for B_y, by either constraining its magnitude or by parametrization. In this section we present figures on a similar format as in sections 2.1, 2.2 and 2.3, only with the roles of B_x and B_y reversed. The purpose is to demonstrate that the techniques are capable of reproducing known variations with B_y, reported in numerous studies [e.g. *Friis-Christensen et al.*, 1984; *Papitashvili et al.*, 2002; *Weimer*, 2001; *Anderson et al.*, 2008; *Green et al.*, 2009; *Friis-Christensen and Wilhjelm*, 1975; *Laundal et al.*, 2016a].

Figure 11 shows the B_y effect according to the empirical models based on CHAMP and *Swarm* (Section 2.1). Figure 12 shows the B_y effect according to AMPERE (see Section 2.2 for details) and Figure 13 shows B_y effects according to the analysis based on SuperMAG ground magnetometers (see Section 2.3).

References

Anderson, B. J., K. Takahashi, and B. A. Toth (2000), Sensing global Birkeland currents with Iridium engineering magnetometer data, *Geophys. Res. Lett.*, *27*, 4045–4048.

Anderson, B. J., H. Korth, C. L. Waters, D. L. Green, and P. Stauning (2008), Statistical Birkeland current distributions from magnetic field observations by the iridium constellation, *Ann. Geophys.*, *26*, 671–687.

Anderson, B. J., H. Korth, D. T. Welling, V. G. Merkin, M. J. Wiltberger, J. Raeder, R. J. Barnes, C. L. W. A. A. Pulkkinen, and L. Rastaetter (2017), Comparison of predictive estimates of high-latitude electrodynamics with observations of global-scale birkeland currents, *Space Weather*, *15*(2), 352–373, doi:10.1002/2016SW001529.

Anderson, E., Z. Bai, C. Bischof, S. Blackford, J. Demmel, J. Dongarra, J. Du Croz, A. Greenbaum, S. Hammarling, A. McKenney, and D. Sorensen (1999), *LAPACK Users' Guide*, third ed., Society for Industrial and Applied Mathematics, Philadelphia, PA.

Backus, G. (1986), Poloidal and toroidal fields in geomagnetic field modeling, *Rev. Geophys.*, *24*, 75–109.

Baker, J. B., A. J. Ridley, V. O. Papitashvili, and C. R. Clauer (2003), The dependence of winter aurora on interplanetary parameters, *J. Geophys. Res.*, *108*, doi:10.1029/2002JA009352.

Cnossen, I., A. D. Richmond, and M. Wiltberger (2012), The dependence of the coupled magnetosphere-ionosphere-thermosphere system on the Earth's magnetic dipole moment, *J. Geophys. Res.*, *117*, doi:10.1029/2012JA017555.

Cowley, S. W. H. (1981), Asymmetry effects associated with the x-component of the IMF in a magnetically open magnetosphere, *Planet. Space Sci.*, *29*(8), 809–818.

Elphinstone, R. D., K. Jankowska, J. S. Murphree, and L. L. Cogger (1990), The configuration of the auroral distribution for interplanetary magnetic field B_z northward 1. IMF B_x and B_y dependencies as observed by the viking satellite, *J. Geophys. Res.*, *95*, 5791–5804.

Finlay, C. C., N. Olsen, S. Kotsiaros, N. Gillet, and L. Tøffner-Clausen (2016), Recent geomagnetic secular variation from Swarm and ground observatories as estimated

in the CHAOS-6 geomagnetic field model, *Earth, Planets and Space*, *68*, 112, doi:
10.1186/s40623-016-0486-1.

Förster, M., Y. I. Feldstein, L. I. Gromova, L. A. Dremukhina, A. E. Levitin, and S. E.
Haaland (2011), Plasma Convection in the High-Latitude Ionosphere Deduced from
Cluster EDI Data and IMF Bx Component, in *Proc. 34th Apatity Annual Seminar
"Physics of Auroral Phenomena", Apatity, 2011*, pp. 42–45.

Friis-Christensen, E., and J. Wilhjelm (1975), Polar cap currents for different directions
of the interplanetary magnetic field in the y-z plane, *J. Geophys. Res.*, *80*, 1248–1260,
doi:10.1029/JA080i010p01248.

Friis-Christensen, E., Y. Kamide, A. D. Richmond, and S. Matsushita (1984), Interplane-
tary Magnetic Field Control of High-Latitude Electric Fields and Currents Determined
From Greenland Magnetometer Data, *J. Geophys. Res.*, *90*, 1325–1338.

Gjerloev, J. W. (2012), The superMAG data processing technique, *J. Geophys. Res.*, *117*,
doi:10.1029/2012JA017683.

Green, D. L., C. L. Waters, B. J. Anderson, and H. Korth (2009), Seasonal and inter-
planetary magnetic field dependence of the field-aligned currents for both Northern and
Southern Hemispheres, *Ann. Geophys.*, *27*, 1701–1715, doi:10.5194/angeo-27-1701-2009.

Haaland, S. E., G. Paschmann, M. Förster, J. M. Quinn, R. B. Torbert, C. E. McIlwain,
H. Vaith, P. A. Puhl-Quinn, and C. A. Kletzing (2007), High-latitude plasma convection
from Cluster EDI measurements: method and IMF-dependence, *Ann. Geophys.*, *25*,
239–253, doi:10.5194/angeo-25-239-2007.

Heppner, J. P., and N. C. Maynard (1987), Empirical high-latitude electric field models,
J. Geophys. Res., *92*, 4467–4489, doi:10.1029/JA092iA05p04467.

Hoilijoki, S., V. M. Souza, B. M. Walsh, P. Janhunen, and M. Palmroth (2014), Magnetopause reconnection and energy conversion as influenced by the dipole tilt and the IMF b_x, *J. Geophys. Res.*, doi:10.1002/2013JA019693.

Huber, P. J. (1964), Robust estimation of location parameter, *Ann. Math. Stat.*, *35*, 73–101.

Iijima, T., and T. A. Potemra (1978), Large-scale characteristics of field-aligned currents associated with substorms, *J. Geophys. Res.*, *83*, 599–615.

Laundal, K. M., and J. W. Gjerloev (2014), What is the appropriate coordinate system for magnetometer data when analyzing ionospheric currents?, *J. Geophys. Res.*, doi:10.1002/2014JA020484.

Laundal, K. M., and N. Østgaard (2009), Asymmetric auroral intensities in the Earth's northern and southern hemispheres, *Nature*, *460*, 491–493, doi:10.1038/nature08154.

Laundal, K. M., and A. D. Richmond (2017), Magnetic Coordinate Systems, *Space Sci. Rev.*, doi:10.1007/s11214-016-0275-y.

Laundal, K. M., J. W. Gjerloev, N. Ostgaard, J. P. Reistad, S. E. Haaland, K. Snekvik, P. Tenfjord, S. Ohtani, and S. E. Milan (2016a), The impact of sunlight on high-latitude equivalent currents, *J. Geophys. Res.*, doi:10.1002/2015JA022236.

Laundal, K. M., C. C. Finlay, and N. Olsen (2016b), Sunlight effects on the 3D polar current system determined from low Earth orbit measurements, *Earth Planets Space*, doi:10.1186/s40623-016-0518-x.

Laundal, K. M., I. Cnossen, S. E. Milan, S. E. Haaland, J. Coxon, N. M. Pedatella, M. Förster, and J. P. Reistad (2017), North-South asymmetries in Earth's magnetic field - Effects on high-latitude geospace, *Space Sci. Rev.*, doi:10.1007/s11214-016-0273-

0.

Matsuo, T., D. J. Knipp, A. D. Richmond, L. Kilcommons, and B. J. Anderson (2015), Inverse procedure for high-latitude ionospheric electrodynamics: Analysis of satellite-borne magnetometer data, *J. Geophys. Res.*, *120*, doi:10.1002/2014JA020565.

Newell, P. T., and J. W. Gjerloev (2011), Evaluation of SuperMAG auroral electro-jet indices as indicators of substorms and auroral power, *J. Geophys. Res.*, *116*, doi: 10.1029/2011JA016779.

Newell, P. T., J. M. Ruohoniemi, and C.-I. Meng (2004), Maps of precipitation by source region, binned by IMF, with inertial convection streamlines, *J. Geophys. Res.*, *109*, doi:10.1029/2004JA010499.

Newell, P. T., T. Sotirelis, K. Liou, C. I. Meng, and F. J. Rich (2007), A nearly univer-sal solar wind-magnetosphere coupling function inferred from 10 magnetospheric state variables, *J. Geophys. Res.*, *112*, doi:10.1029/2006JA012015.

Ohtani, S., S. Wing, G. Ueno, and T. Higuchi (2009), Dependence of premidnight field-aligned currents and particle precipiation on solar illumination, *J. Geophys. Res.*, *114*, doi:10.1029/2009JA014115.

Olsen, N. (1997), Ionospheric F region currents at middle and low latitudes estimated from Magsat data, *J. Geophys. Res.*, *102*, 4563–4576.

Østgaard, N., S. B. Mende, H. U. Frey, L. A. Frank, and J. B. Sigwarth (2003), Observations of non-conjugate theta aurora, *Geophys. Res. Lett.*, *30*, doi: 10.1029/2003GL017914.

Papitashvili, V. O., F. Christiansen, and T. Neubert (2002), A new model of field-aligned currents derived from high-precision satellite magnetic field data, *Geophys. Res. Lett.*,

29, doi:10.1029/2001GL014207.

Park, K. S., T. Ogino, and R. J. Walker (2006), On the importance of antiparallel reconnection when the dipole tilt and IMF B_y are nonzero, *J. Geophys. Res.*, *111*, doi: 10.1029/2004JA010972.

Parker, E. N. (1958), Dynamics of the interplanetary gas and magnetic fields, *Astrophysical Journal*, *128*, 664–676, doi:10.1086/146579.

Peng, Z., C. Wang, and Y. Q. Hu (2010), Role of IMF Bx in the solar wind-magnetosphere-ionosphere coupling, *J. Geophys. Res.*, *115*, doi:10.1029/2010JA015454.

Pettigrew, E. D., S. G. Shepherd, and J. M. Ruohoniemi (2010), Climatological patterns of high-latitude convection in the Northern and Southern hemispheres: Dipole tilt dependencies and interhemispheric comparison, *J. Geophys. Res.*, *115*, doi: 10.1029/2009JA014956.

Reistad, J. P., N. Østgaard, K. M. Laundal, and K. Oksavik (2013), On the non-conjugacy of nightside aurora and their generator mechanisms, *J. Geophys. Res.*, doi:10.1002/J. Geophys. Res.a.50300.

Reistad, J. P., N. Østgaard, K. M. Laundal, S. Haaland, P. Tenfjord, K. Snekvik, K. Oksavik, and S. E. Milan (2014), Intensity asymmetries in the dusk sector of the poleward auroral oval due to IMF Bx, *J. Geophys. Res.*, doi:10.1002/2014JA020216.

Richmond, A. D. (1995a), Ionospheric electrodynamics using magnetic apex coordinates, *J. Geomag. Geoelectr.*, *47*, 191–212.

Richmond, A. D. (1995b), Ionospheric electrodynamics, in *Handbook of Atmospheric Electrodynamics, Volume II*, edited by H. Volland, pp. 249–290, CRC Press.

Russell, C. T., and R. L. McPherron (1973), Semiannual variation of geomagnetic activity, *Journal of Geophysical Research*, *78*(1), 92–108, doi:10.1029/JA078i001p00092.

Russell, C. T., Y. L. Wang, and J. Raeder (2003), Possible dipole tilt dependence of dayside magnetopause reconnection, *Geophys. Res. Lett.*, *30*, doi:10.1029/2003GL017725.

Sabaka, T. J., G. Hulot, and N. Olsen (2010), *Handbook of Geomathematics*, chap. Mathematical Properties Relevant to Geomagnetic Field Modeling, pp. 503–538, Springer Berlin Heidelberg, Berlin, Heidelberg, doi:10.1007/978-3-642-01546-5_17.

Shi, Q. Q., Q.-G. Zong, S. Y. Fu, M. W. Dunlop, Z. Y. Pu, G. K. Parks, Y. Wei, W. H. Li, H. Zhang, M. Nowada, Y. B. Wang, W. J. Sun, T. Xiao, H. Reme, C. Carr, A. N. Fazakerley, and E. Lucek (2013), Solar wind entry into the high-latitude terrestrial magnetosphere during geomagnetically quiet times, *Nature communications*, *4*, 1466.

Shue, J.-H., P. T. Newell, K. Liou, and C. I. Meng (2001), Influence of interplanetary magnetic field on global auroral patterns, *J. Geophys. Res.*, *106*, 5913–5926.

Shue, J.-H., P. T. Newell, K. Liou, C.-I. Meng, and S. W. H. Cowley (2002), Interplanetary magnetic field B_x asymmetry effect on auroral brightness, *J. Geophys. Res.*, *107*, doi: 10.1029/2001JA000229.

Stenbaek-Nielsen, H. C., E. M. Wescott, T. N. Davis, and R. W. Peterson (1973), Differences in auroral intensity at conjugate points, *J. Geophys. Res.*, *78*, 659–671.

Tenfjord, P., and N. Østgaard (2013), Energy transfer and flow in the solar wind-magnetosphere-ionosphere system: A new coupling function, *J. Geophys. Res.*, *118*, 5659–5672, doi:10.1002/jgra.50545.

Tenfjord, P., N. Østgaard, K. Snekvik, K. M. Laundal, J. P. Reistad, S. Haaland, and S. Milan (2015), How the IMF By induces a By component in the closed magnetosphere

and how it leads to asymmetric currents and convection patterns in the two hemispheres, *J. Geophys. Res.*, doi:10.1002/2015JA02157.

Waters, C. L., B. J. Anderson, and K. Liou (2001), Estimation of global field aligned currents using the iridium system magnetometer data, *Geophys. Res. Lett.*, *28*, 2165–2168.

Weimer, D. (2001), Maps of ionospheric field-aligned currents as a function of the interplanetary magnetic field derived from Dynamics Explorer 2, *J. Geophys. Res.*, *106*, 12,889–12,902.

Weimer, D. R. (2013), An empirical model of ground-level geomagnetic perturbations, *Space Weather*, *11*, 107–120, doi:10.1002/swe.20030.

Wilcox, J. M., and N. F. Ness (1965), Quasi-stationary corotating structure in the interplanetary medium, *Journal of Geophysical Research*, *70*(23), 5793–5805, doi: 10.1029/JZ070i023p05793.

Zhao, H., and Q.-G. Zong (2012), Seasonal and diurnal variation of geomagnetic activity: Russell-mcpherron effect during different imf polarity and/or extreme solar wind conditions, *Journal of Geophysical Research: Space Physics*, *117*(A11), doi: 10.1029/2012JA017845, a11222.

Zhu, C. B., H. Zhang, Y. S. Ge, Z. Y. Pu, W. L. Liu, W. X. Wan, L. B. Liu, Y. D. Chen, H. J. Le, and Y. F. Wang (2015), Dipole tilt angle effect on magnetic reconnection locations on the magnetopause, *J. Geophys. Res.*, doi:10.1002/2015JA020989.
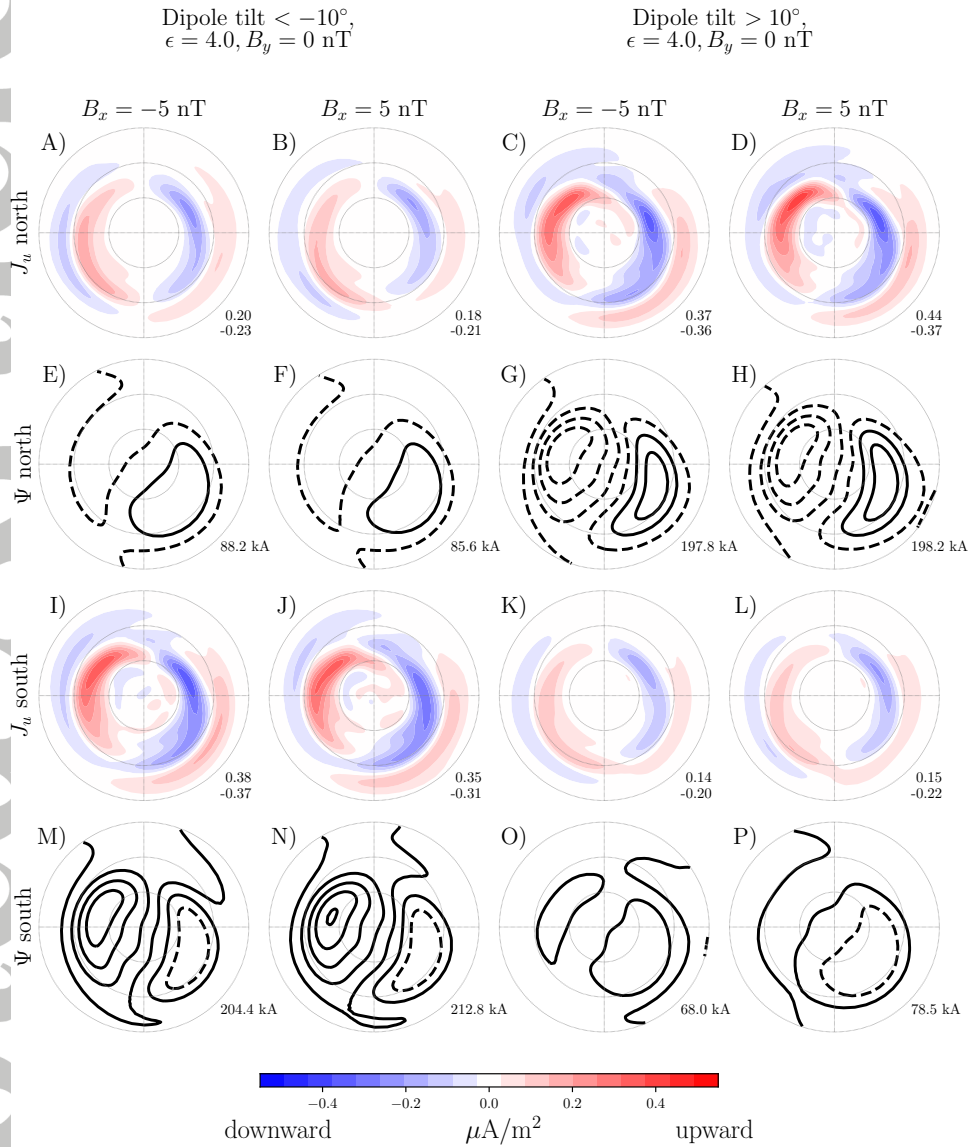
Figure 1. Birkeland currents (color) and horizontal equivalent currents (black contours) from two different empirical models of ionospheric currents, based on magnetic field measurements from the CHAMP and *Swarm* satellites. The two left columns are based on data from periods when the dipole tilt angle was $< -10°$, and the right columns on periods when the tilt angle was $> 10°$. The models depend on both B_x and B_y, and in this figure we set $B_y = 0$ to highlight any B_x effect. The *Newell et al.* [2007] coupling function ϵ is set to 4. Numbers in the lower right corner of the Birkeland current plots indicate peak upward (positive) and downward (negative) currents, in $\mu A/m^2$. The number in the lower right corner of the equivalent current plots indicate the total current flowing between the maximum and minimum of the current function. 30 kA flow between each contour.
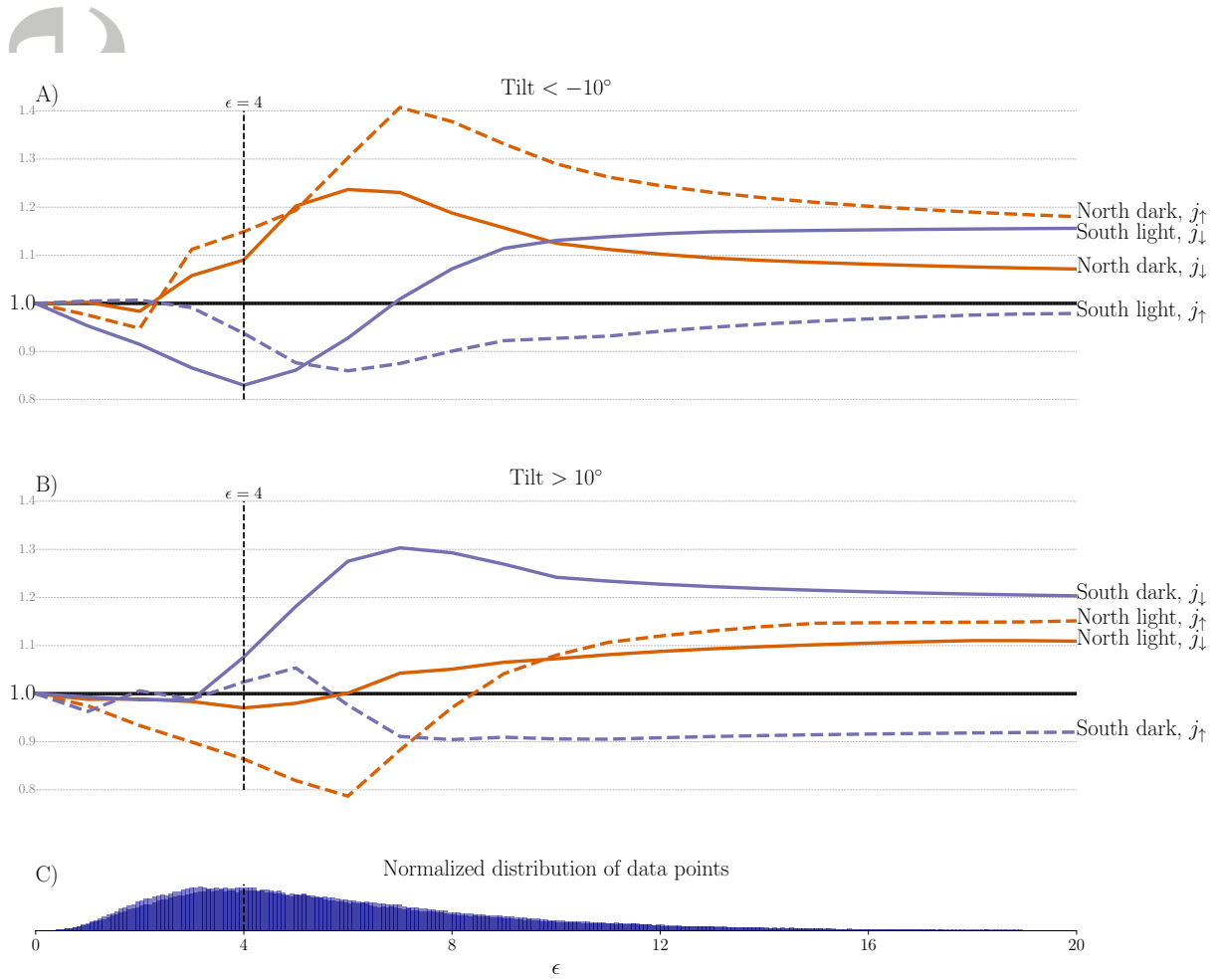
Figure 2. Ratios of corresponding R1 currents for different signs of B_x, as a function of ϵ. The ratios are defined such that they are > 1 if the asymmetry is consistent with the *Reistad et al.* [2014] predictions. The curves for the two models are shown separately in A (tilt $< -10°$) and B (tilt $> 10°$). The normalized distribution of ϵ is shown in C. The distributions for the two models overlap where the color is dark blue.
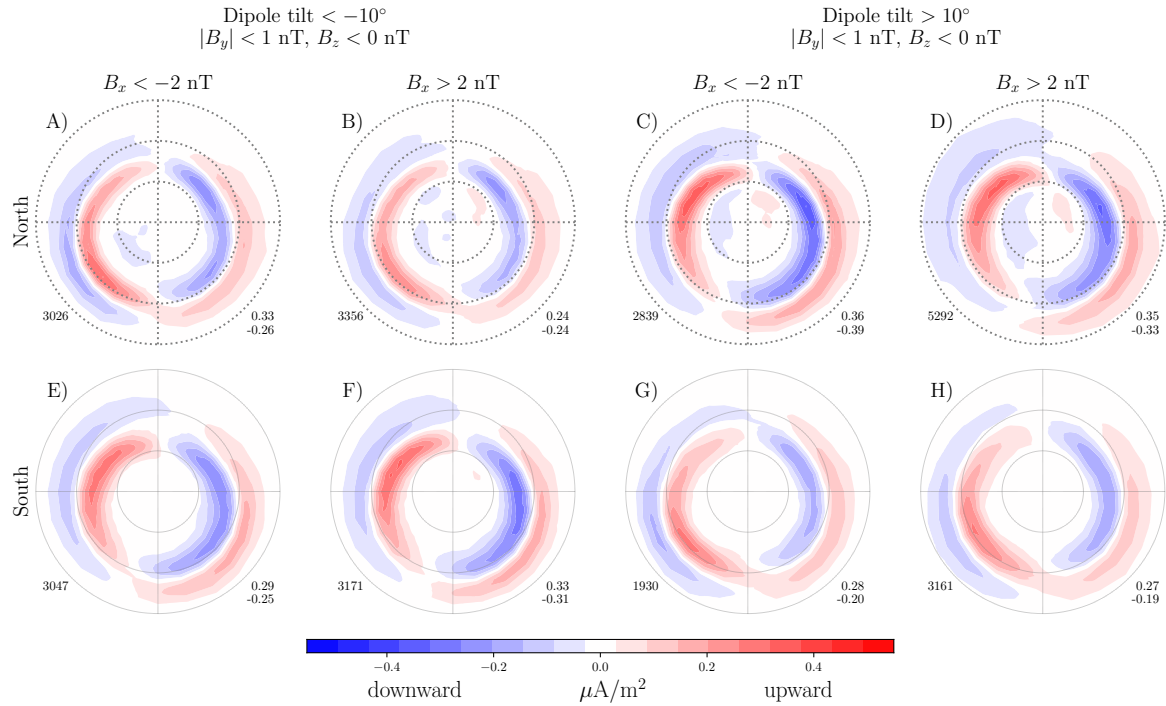
Figure 3. Maps of average AMPERE Birkeland currents from both hemispheres during B_z negative/B_x-dominated conditions. The northern hemisphere is shown in the upper row and the southern hemisphere in the lower row. The plots in the two columns to the left are based on data from periods when the tilt angle was $< -10°$, and the right plots on periods when the tilt was $> 10°$.
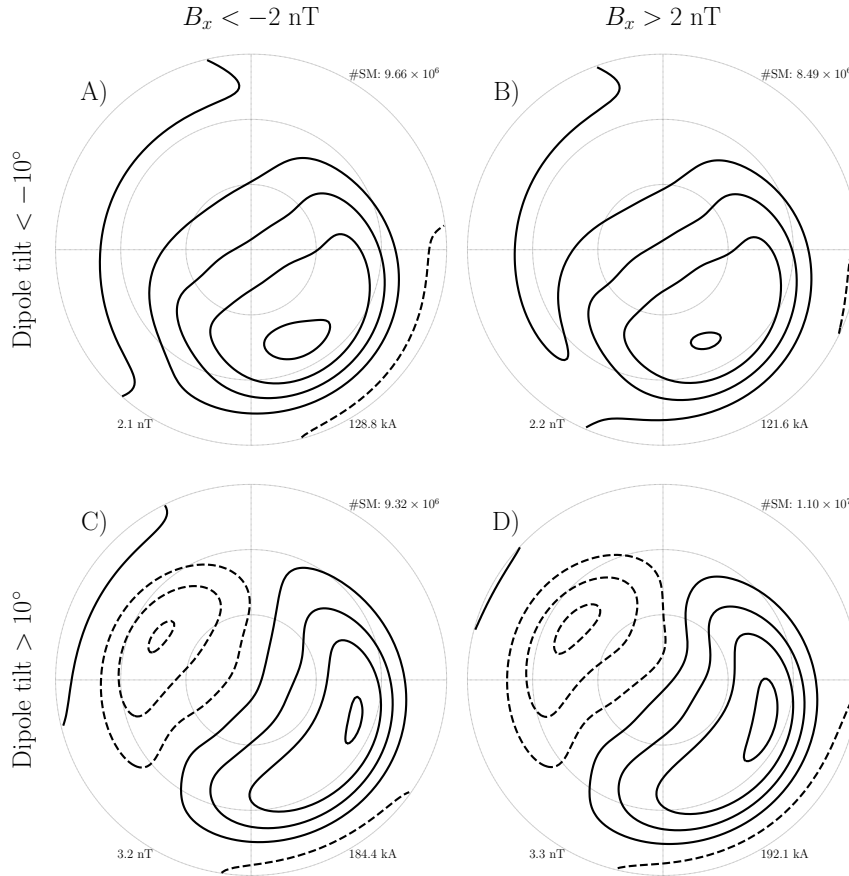
Figure 4. Equivalent current patterns derived from northern hemisphere ground based magnetometer measurements in the period 1981-2014, obtained when $B_z < -1$ and $|B_y| < 1$ nT. IMF $B_x > 2$ in the left column and $B_x < -2$ nT in the right column. In the top row, the dipole tilt angle is $> 10°$ (summer) and the bottom row it is $< -10°$ (winter). A full description of the technique is given in *Laundal et al.* [2016a]. 30 kA contour spacing.
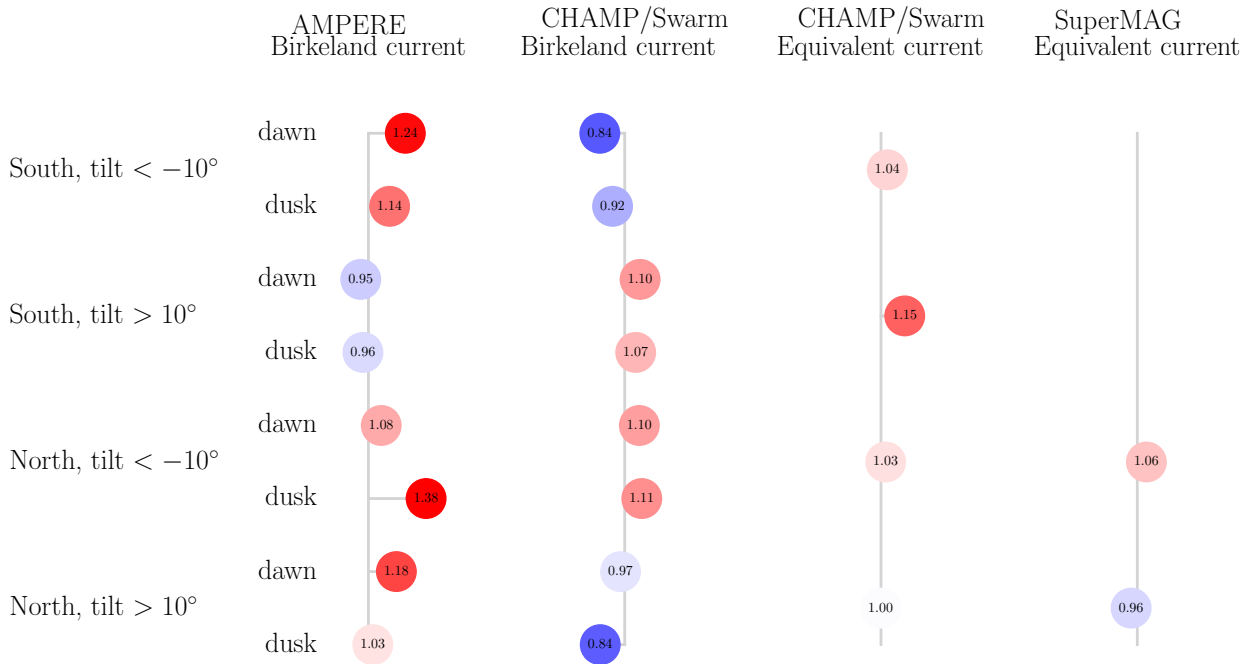
	AMPERE Birkeland current	CHAMP/Swarm Birkeland current	CHAMP/Swarm Equivalent current	SuperMAG Equivalent current
South, tilt $< -10°$ dawn	1.24	0.84	1.04	
dusk	1.14	0.92		
South, tilt $> 10°$ dawn	0.95	1.10	1.15	
dusk	0.96	1.07		
North, tilt $< -10°$ dawn	1.08	1.10	1.03	1.06
dusk	1.38	1.11		
North, tilt $> 10°$ dawn	1.18	0.97	1.00	0.96
dusk	1.03	0.84		

Figure 5. The ratios of corresponding currents during presumably favourable IMF B_x conditions to unfavourable conditions (numbers > 1 indicate that the asymmetry is consistent with the predictions by *Reistad et al.* [2014]). Birkeland current ratios are based on the peak values listed in figures 1 and 3. For the equivalent currents, the ratios are based on the total current, listed in Figures 1 and 4.
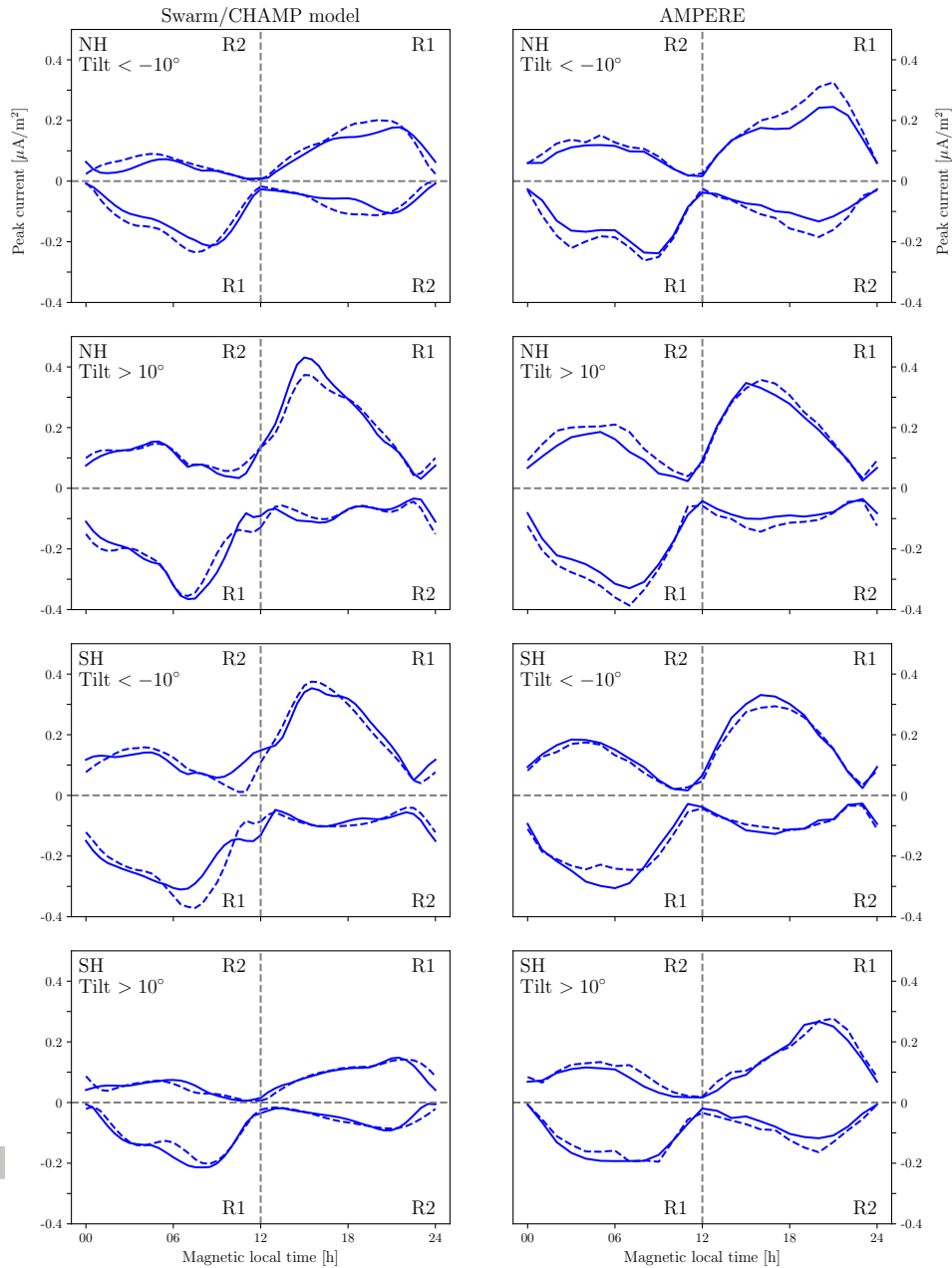
Figure 6. Peak upward and downward currents (positive and negative, respectively) as a function of MLT. Solid blue curves show results for positive B_x and dashed for negative. The values in the left column correspond to the plots in Figure 1, which shows maps based on the *Swarm*/CHAMP models. The values in the right column correspond to the plots in Figure 3, based on AMPERE. The four quadrants are labeled by the current that contributes to the values there (R1 or R2). Tilt angle domain and hemisphere are indicated in the top left corners.

AL vs |B_x| (binned average, 1990-2016) with different tilt angles
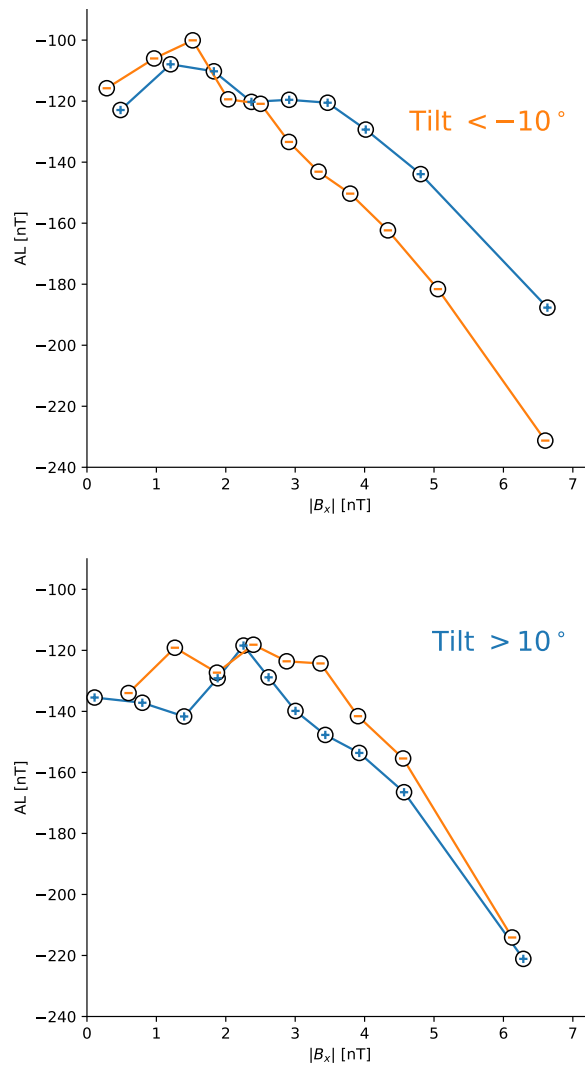

Figure 7. Average AL as a function of average $|B_x|$, in bins defined by quantiles of B_x during conditions defined by $B_z < -1$ nT, $|B_y| < 1$ nT, and dipole tilt $< -10°$ (top) or $> 10°$ (bottom). In each plot, the two curves correspond to different signs of B_x, with blue color indicating positive B_x and orange color indicating negative B_x. AL tends to be stronger (more negative) when B_x and dipole tilt have the same sign.
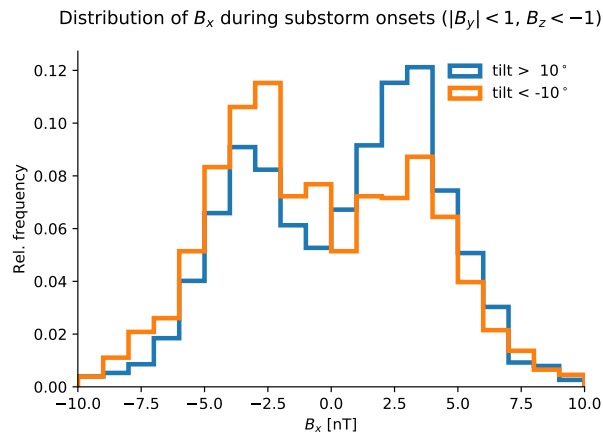
Distribution of B_x during substorm onsets ($|B_y| < 1$, $B_z < -1$)

Figure 8. The distributions of IMF B_x at substorm onsets that occurred when $|B_y| < 1$ nT, $B_z < -1$ nT, and the dipole tilt angle was either $> 10°$ (blue) or $< -10°$ (orange). Each histogram is based on slightly more than 1500 onsets, from a list of more than 62,000 substorms provided by SuperMAG (1981-2015).
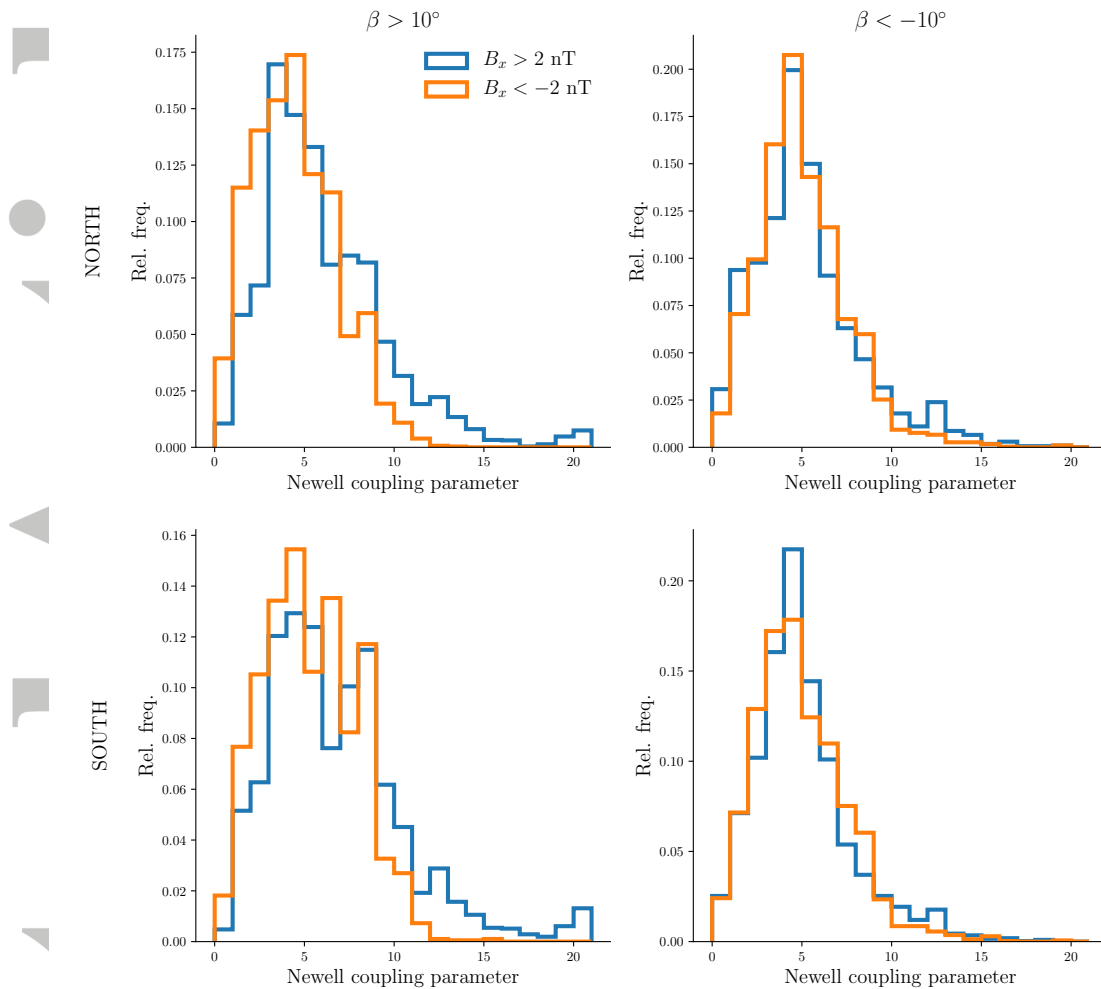
Figure 9. The distribution of *Newell et al.* [2007]'s coupling parameter (ϵ in equation 2) for the AMPERE current maps used to make Figure 3. Each plot corresponds to one hemisphere (upper row: North, lower row: South) and tilt angle (left column: Positive tilt, right column: Negative tilt), and the two histograms in each plot correspond to different B_x bins (blue: $B_x > 2$ nT, orange: $B_x < -2$ nT).
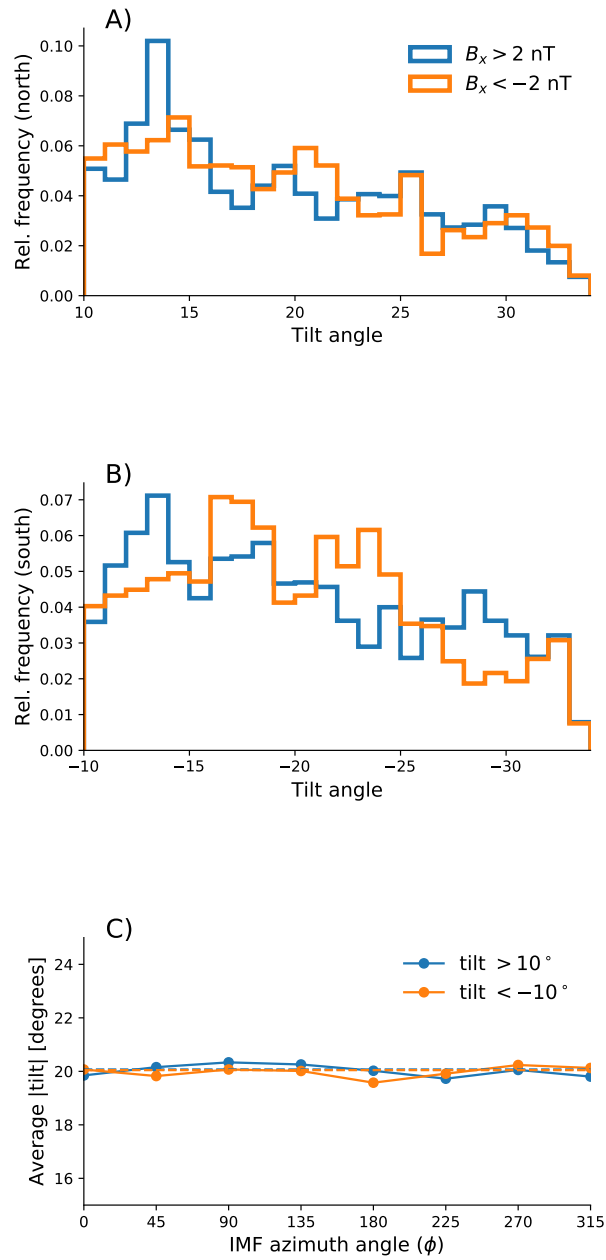
Figure 10. A and B: Distributions of the dipole tilt angle at the times of the AMPERE maps that were used to produce Figure 3. Panel A correspond to maps in the northern hemisphere during positive tilt, and panel B to maps in the southern hemisphere during negative tilt. Different colors correspond to different signs of B_x. C) the weighted mean tilt angle in $45°$ wide bins of IMF azimuth angle, at the times of the CHAMP/*Swarm* data used to produce figure 1. The weights used to calculate the means are the final Huber weights in the iterative scheme to estimate the spherical harmonic models described in Section 2.1.
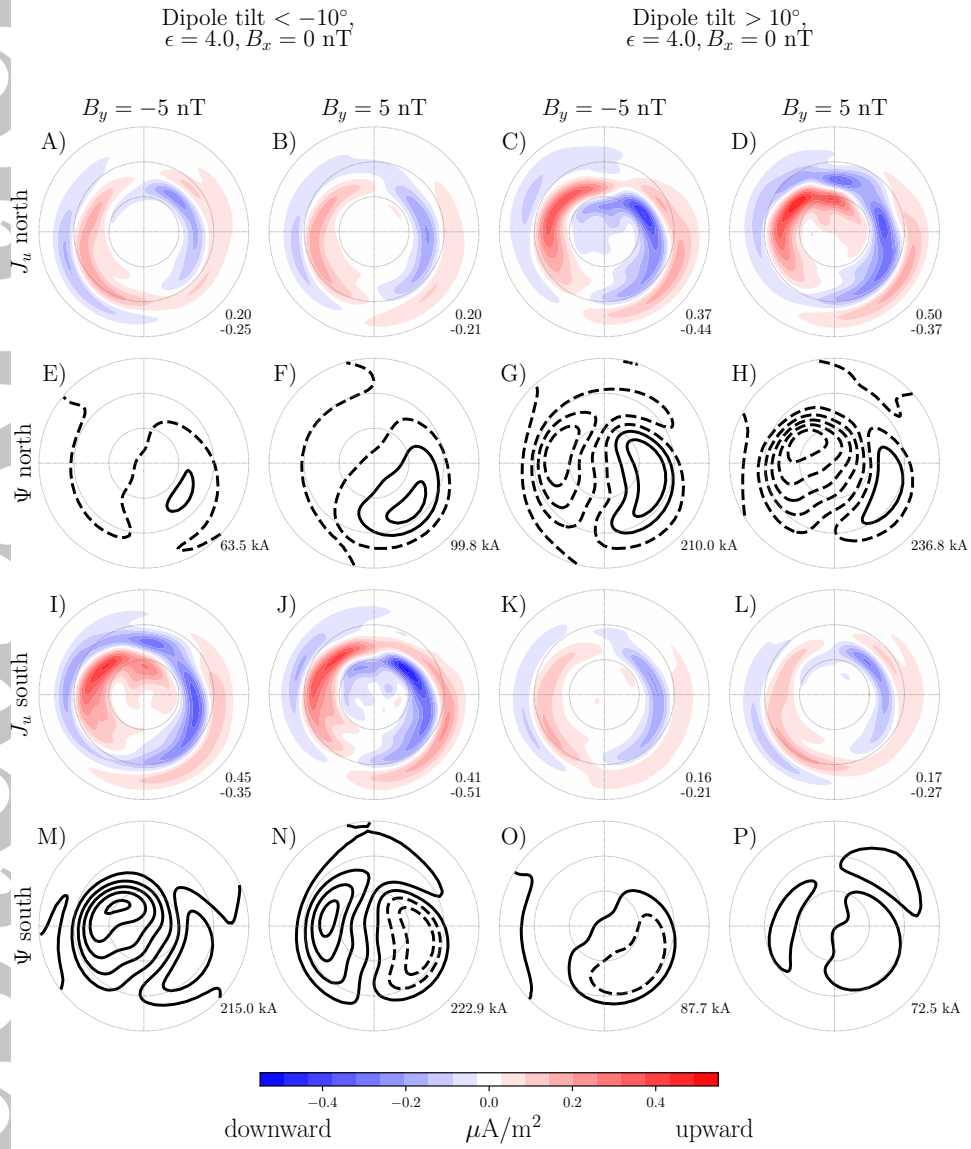
Dipole tilt $< -10°$,
$\epsilon = 4.0, B_x = 0$ nT

Dipole tilt $> 10°$,
$\epsilon = 4.0, B_x = 0$ nT

$B_y = -5$ nT $B_y = 5$ nT $B_y = -5$ nT $B_y = 5$ nT

Figure 11. Same as Figure 1, only with the roles of B_x and B_y reversed

Dipole tilt $< -10°$
$|B_x| < 1$ nT, $B_z < 0$ nT

Dipole tilt $> 10°$
$|B_x| < 1$ nT, $B_z < 0$ nT

$B_y < -2$ nT $B_y > 2$ nT $B_y < -2$ nT $B_y > 2$ nT
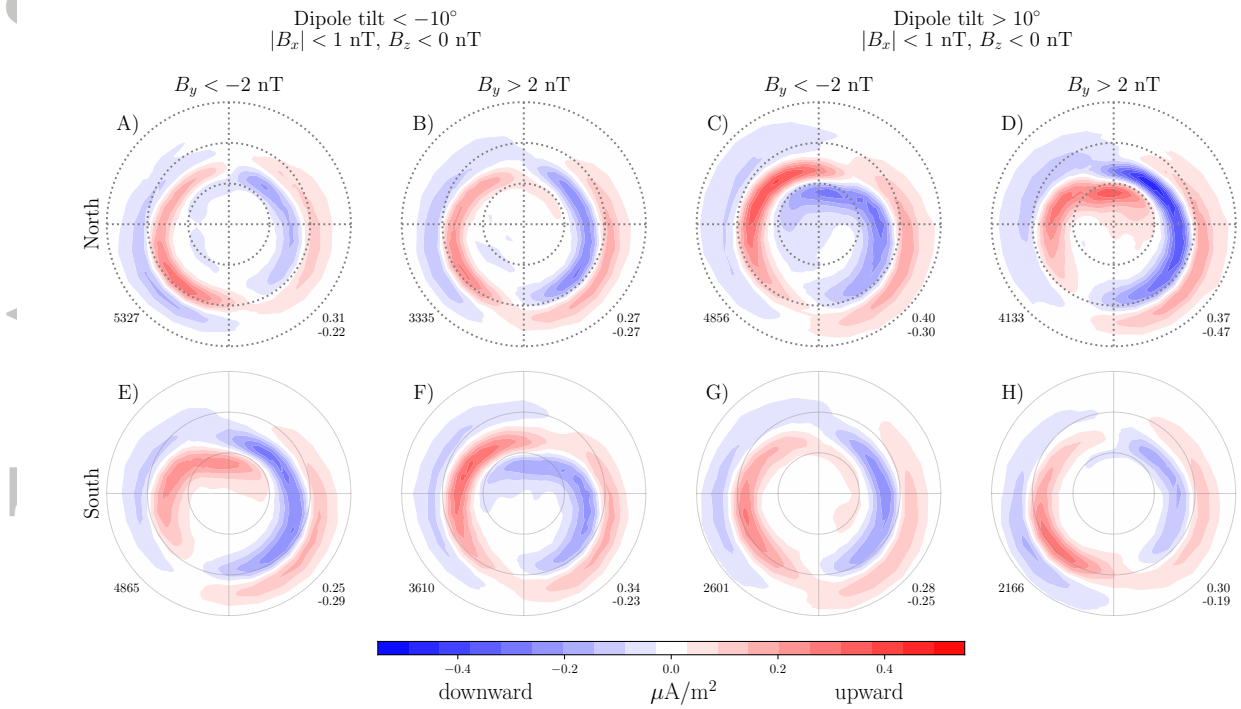
Figure 12. Same as Figure 3, only with the roles of B_x and B_y reversed

$B_y < -2$ nT $\quad\quad\quad\quad\quad$ $B_y > 2$ nT

A) #SM: 8.88×10^6

B) #SM: 8.98×10^6

Dipole tilt $< -10°$

2.0 nT $\quad\quad$ 113.2 kA

2.3 nT $\quad\quad$ 161.2 kA

C) #SM: 1.06×10^7

D) #SM: 8.90×10^6

Dipole tilt $> 10°$

3.6 nT $\quad\quad$ 254.4 kA
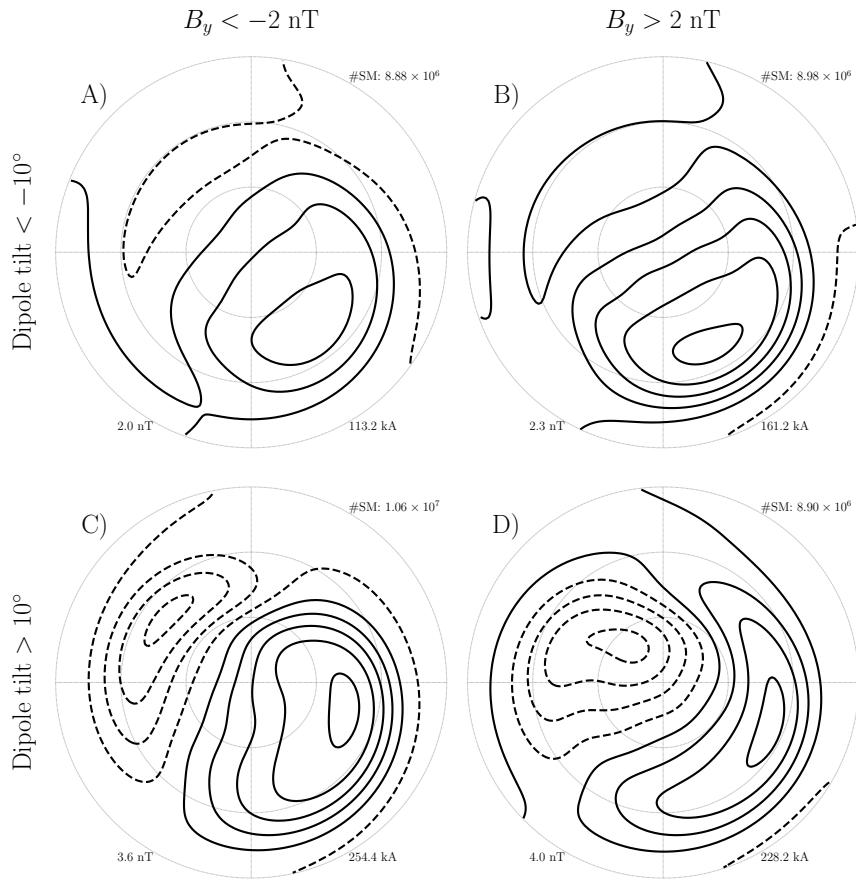
4.0 nT $\quad\quad$ 228.2 kA

Figure 13. Same as Figure 4, only with the roles of B_x and B_y reversed